Nonlocal correlation mediated by Weyl orbits

Zhe Hou [1] and Qing-Feng Sun [1,2,3,*]

[1] International Center for Quantum Materials, School of Physics, Peking University, Beijing 100871, China
[2] Collaborative Innovation Center of Quantum Matter, Beijing 100871, China
[3] CAS Center for Excellence in Topological Quantum Computation, University of Chinese Academy of Sciences, Beijing 100190, China

(Received 1 February 2020; accepted 6 May 2020; published 27 May 2020)

Nonlocality is an interesting topic in quantum physics and is usually mediated by some unique quantum states. Here we investigate a Weyl semimetal slab and find an exotic nonlocal correlation effect when placing two potential wells merely on the top and bottom surfaces. This correlation arises from the peculiar Weyl orbit in Weyl semimetals and is a consequence of the bulk-boundary correspondence in topological band theory. A giant nonlocal transport signal and a body breakdown by Weyl fermions are further uncovered, which can serve as signatures for verifying this nonlocal correlation effect experimentally. Our results extend another member in the nonlocality family and have potential applications for designing unique electric devices with fancy functions.

DOI: 10.1103/PhysRevResearch.2.023236

I. INTRODUCTION

Nonlocality has always been an intriguing topic in quantum physics. The most famous example is the quantum entanglement [1,2] of two or more particles concerning their spin, momentum, or position in the entangled state. The quantum entanglement violates the Bell inequality [3,4], comes along with a spooky action at a distance [5], and has been utilized for quantum dense encoding [6] and information teleportation [7]. In solid state materials, nonlocality also exists in some zero mode excitations whose properties mimic the fundamental particles in quantum field theory, such as the Majorana zero modes in a p-wave superconductor chain [8–10] and the Jackiw-Rebbi zero mode in a quantum spin Hall insulator constriction [11–13]. Conceptually the zero modes can be regarded as half an intact particle and, similar to the positive and negative monopoles in a magnet, they have an intrinsic nonlocal correlation and can only create or annihilate in pairs.

Basically in a nonlocal phenomenon, applying a perturbation at one site of the system could arouse a remote response at the other site, which realizes a "communication" between particles over long distances. Yet nonlocality of fermion in three dimensional bulk materials are rarely reported. The main reason stems from the electrostatic screening to the perturbation and the overall distribution of the bulk wave functions, which make the spatial response decay exponentially or proportionally to r^{-3} with the distance r [14]. Recently a series of unconventional quantum oscillations in topological Dirac semimetals Cd_3As_2 were reported in experiments [15–17]. In those systems, there exists a closed orbit in momentum space connecting the surface and bulk states, namely the Weyl orbit. Under the magnetic field, Weyl fermions can move along the Weyl orbit and tunnel between the top and bottom surfaces through the bulk states. The bulk and surface connection by the Weyl orbit implies that there may exist a deeper and intrinsic nonlocality in topological semimetals.

Here we report a three dimensional nonlocal correlation effect in topological Weyl semimetals (WSMs) [18–24]. We show that by putting two attractive potential wells (PWs) merely on the top and bottom surfaces, a giant intersurface correlation across the body would happen. The PW in the WSM works as a particle beam deflector which injects the Weyl fermions on the surface into the bulk or extracts them from the bulk to the surface. With both PWs, the surface Weyl fermions would first be pumped into the bulk and then appear on the other surface, which realizes a remote nonlocal correlation between the PWs. This phenomenon arises from the unique band structure, i.e., the Weyl orbit, and is an intrinsic property in WSMs because no externally global electric or magnetic fields are applied. For Weyl fermions taking a round trip between the top/bottom surface and obtaining a $2n\pi$ phase with the integer n, a stationary bridge state along with a body breakdown inside the WSM would happen, which can be a strong signature for the experimental verification on the remote correlation effect.

This paper is organized as follows. In Sec. II, we introduce the model of our setup and explain the mechanism of the nonlocal correlation mediated by the Weyl orbits. In Sec. III, we present two results which arise from the nonlocal correlation: the response of the density of states and the enhancement of the nonlocal transport. In Sec. IV we give a semiclassical description on the trajectories of the Weyl fermions. In Sec. V we discuss the details on experimentally verifying the nonlocal correlation and make a conclusion for our results.

*sunqf@pku.edu.cn

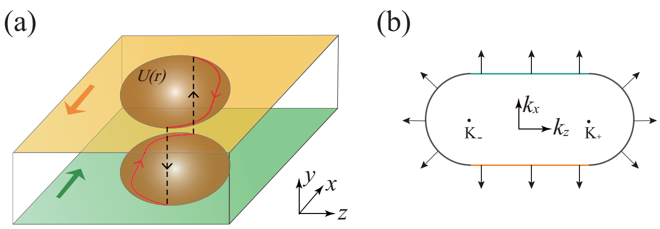

FIG. 1. Schematic diagram of the nonlocal intersurface correlation mediated by the Weyl orbit. (a) The real space trajectory of the Weyl fermions in the WSM slab with an elliptical PW (the brown circle) on the top and bottom surfaces. The slab is infinitely large in x and z directions but has a thickness $N_y a$ in y direction. (b) The Weyl orbit in the momentum space for the WSM slab in (a). Here the up and down line segments denote the bottom and top surface states, respectively. The black half circles denote the trivial bulk states which are connected with the surface states near the Weyl nodes. The black arrows on the Weyl orbit indicate the directions of the group velocity.

II. MODEL

We consider a WSM slab which is infinitely large in x and z directions but has finite width (N_y layers) in y direction, as shown in Fig. 1(a). The Hamiltonian of the WSM has a two band form [25–27]: $\hat{H}=\sum_{\mathbf{k}} c_{\mathbf{k}}^{\dagger}H(\mathbf{k})c_{\mathbf{k}}$ with $c_{\mathbf{k}}=(c_{\mathbf{k}\uparrow},c_{\mathbf{k}\downarrow})^T$ and $H(\mathbf{k})=t_z\sigma_z(2+\gamma-\cos k_x a-\cos k_y a-\cos k_z a)+t_x\sigma_x\sin k_x a+t_y\sigma_y\sin k_y a$. Here $\mathbf{k}$ is the wave vector, a is the lattice constant, and $t_i(i=x,y,z)$ is the hopping energy of nearest sites in the i direction. The Pauli matrix σ_i acts on the spin space. Here the electron-electron interaction has been ignored in the Hamiltonian, because some experiments have shown that the electron-electron interaction is weak in WSM [16,17]. In addition, the nonlocal correlation effect that we suggest originates from the Weyl orbits, not from the interaction. In this model, there exist two Weyl nodes locating at $\mathbf{K}_{\pm}=(0,0,\pm k_0)$ with $\cos k_0 a=\gamma$ in the Brillouin zone. The Weyl node plays the role of magnetic monopoles with positive or negative chirality in the momentum space, and due to the bulk-boundary correspondence, the chiral surface states are formed in the WSM slab sketched in Fig. 1(a) and propagate in $\pm x$ direction in the bottom (top) surface, as shown with the yellow and green arrows. With equal energies, the surface states cannot get closed themselves in momentum space but have to transit into bulk states near the Weyl nodes, which constitute a closed loop, i.e., the Weyl orbit in Fig. 1(b).

Next we show how the applied PWs induce a nonlocal intersurface response within the Weyl orbit regime. The dark brown circles in Fig. 1(a) indicate the PWs which are on the same position of the top/bottom surfaces and yield an elliptical form: $U(\mathbf{r})=\omega_x(x-x_C)^2+\omega_z(z-z_C)^2-\omega_x r_0^2$, if $\omega_x(x-x_C)^2+\omega_z(z-z_C)^2\leqslant\omega_x r_0^2$ and $y=0,N_y a$. For other positions the potential is assumed to be zero. Here $(x_C,z_C),\omega_{x,z}$ and r_0 are the central position, strength, and size of the PW, respectively. Similar to a magnetic field, the attracting potential providing an electrostatic force $\mathbf{F}=-\nabla U(r)$ alters the moving trajectory of Weyl fermions and forces them into closed orbits. However, different from the electrons in normal 2D electron gas or the Dirac fermions on the surface of 3D topological insulators [28], Weyl fermions cannot be simply confined on the WSM surfaces due to the unidirectional propagation of the topological surface states [see the yellow and green segments in Fig. 1(b)].

For the Weyl fermion residing on the top surface states with a group velocity pointing in $-x$ direction, once it is trapped inside the quantum dot like PW [see Fig. 1(a)], the attractive electrostatic force tries to change its real space trajectory (the top red curve) and meanwhile the $-z$ component pushes it into the bulk states in the momentum space [the left black half circle in Fig. 1(b)]. The velocity is then tilted in the $-z$ direction and the real space trajectory is deflected to the left. The wave function which first localizes on the top surface starts to permeate into the body region (see Appendix A), and the central position of the Weyl fermion moves down as shown with the dotted black line in Fig. 1(a).

If there exists only one PW on the top surface, the Weyl fermion is merely pumped into the body region and stops moving downward to affect the bottom surface, while if the bottom PW is placed as well, the electrostatic force would continue driving the Weyl fermion already in the body and pumps them into the bottom surface. The wave function is then pushed from the bulk states into the bottom surface states with a group velocity in x direction [the bottom red curve in Fig. 1(a)]. For the Weyl fermion pumped from the bottom surface into the top one, a similar statement can be made. Thus the Weyl fermion accomplishes half a circular motion in both top/bottom surfaces under the drive of PWs. This results in a nonlocal correlation which is formed between the top and bottom PWs and mediated by the bulk states inside the Weyl orbit.

III. NONLOCAL RESPONSE DRIVEN BY THE SURFACE PWs

A. Response of the density of states

To verify the nonlocal correlation discussed above, we conceive four infinitely long WSM nanoribbon systems as shown in Figs. 2(a)–2(d) and calculate the response of the density of states (DOS) inside the nanoribbons. In Fig. 2(a) a pure nanoribbon with no PWs is shown, but in Figs. 2(b), 2(c), and 2(d) the PW is put on the bottom, top, and top/bottom surfaces, respectively. To eliminate that the surface states bypass the side walls and reach the other surface due to their helicity, we set the nanoribbons infinitely long in x direction and restrict them in y and z directions with N_y and N_z layers. We first rewrite the Weyl Hamiltonian $\hat{H}$ in the tight-binding form

$$\hat{H}=\sum_i[c_i^{\dagger}T_0c_i+c_i^{\dagger}T_xc_{i+\delta\mathbf{x}}+c_i^{\dagger}T_yc_{i+\delta\mathbf{y}}+c_i^{\dagger}T_zc_{i+\delta\mathbf{z}}+\mathrm{H.c.}] \tag{1}$$

by performing the Fourier transformations $c_i=\frac{1}{\sqrt{N}}\sum_{\mathbf{k}}e^{i\mathbf{k}\cdot\mathbf{r}_i}c_{\mathbf{k}}$ with $c_i=(c_{i\uparrow},c_{i\downarrow})^T$. Here $c_{i\uparrow}(c_{i\downarrow})$ is the annihilation operator at site i with spin $\uparrow$ ($\downarrow$), N is the total site number of the system, and $\mathbf{r}_i$ is the position of site i. The

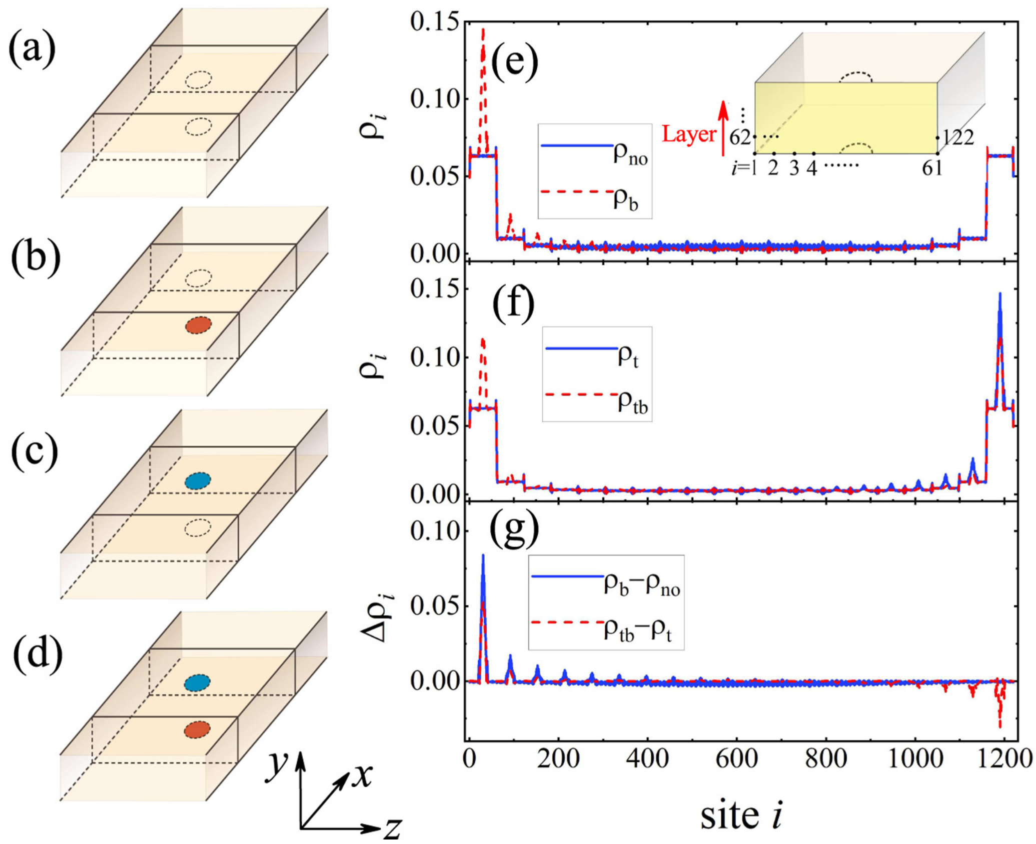

FIG. 2. Nonlocal DOS response in WSM nanoribbons. (a)–(d) Four infinitely long WSM nanoribbons (along x direction) with no PWs (a), top PW (b), bottom PW (c), and top/bottom PWs (d) on the surface. (e) The DOS $\rho_{\rm no}$ and $\rho_{\rm b}$ of the center section (the bright region in the subfigure) for the nanoribbon in (a) and (b). Here the site i counts from the left to the right, and then from the bottom to the top. (f) The DOS $\rho_{\rm t}$ and $\rho_{\rm tb}$ of the center section for the nanoribbon in (c) and (d). (g) The DOS response $\rho_{\rm b}-\rho_{\rm no}$ and $\rho_{\rm tb}-\rho_{\rm t}$. For (e)–(g) we set the energy $E=0.2t$. Throughout the paper we set $N_y=20,\ N_z=61,\ \gamma=0,\ t_x=t_y=t_z=t,\ r_0=10a,\ \omega_x=0.004t/a^2,\ \omega_z=0.01t/a^2$, and $\eta=0.001i$. The central position of the PWs is put on the center of the WSM slab surface.

T matrices in Eq. (1) are

$$T_0=\begin{pmatrix}2t_z+2\gamma & 0\\ 0 & -2t_z-2\gamma\end{pmatrix},\quad T_x=\begin{pmatrix}-t_z/2 & t_x/2i\\ t_x/2i & t_z/2\end{pmatrix},$$
$$T_y=\begin{pmatrix}-t_z/2 & -t_y/2\\ t_y/2 & t_z/2\end{pmatrix},\quad T_z=\begin{pmatrix}-t_z/2 & 0\\ 0 & t_z/2\end{pmatrix}. \tag{2}$$

In calculating the DOS, we divide the slab into three regions: left infinitely long nanoribbon (with Hamiltonian H_L), the central region (with Hamiltonian H_C), and right infinitely long nanoribbon (with Hamiltonian H_R). The two infinitely long nanoribbons satisfy the Hamiltonian in Eq. (1) and have a surface Green's function $\mathbf{g}^S_{L(R)}(E)$ for the left (right) terminal. The central region contains the surface PW $U(\mathbf{r})$ and its Green's function can be obtained as $\mathbf{G}^r_C(E)=[(E+\eta t)\mathbf{I}-H_C-\sum_{m=L,R}\Sigma^r_m]^{-1}$. Here η is an imaginary number and Σ^r_m is the self-energy of terminal m, which is calculated as $\Sigma^r_m=H_{Cm}\mathbf{g}^S_m H_{mC}$, where $H_{Cm}(H_{mC})$ denotes the coupling between the central region and terminal m. The DOS at site i in the central region is obtained by taking the imaginary part of the Green's function:

$$\rho_i(E)=-\mathrm{Im}\mathbf{G}^r_C(i,E)/\pi. \tag{3}$$

Figure 2(e) gives the DOS ρ_i of the central section with and without the bottom PW. Here the energy E is chosen to be $0.2t$ above the Weyl node and the Fermi surface is a single Weyl orbit with no second bulk states mixing in. As can be seen from the no-potential case (the blue curve $\rho_{\rm no}$), the DOS dominates in the top/bottom surfaces and decays quickly into a stable distribution away about three layers. The nonzero ρ_i in the body arises from the few bulk states in the Weyl orbit. After the bottom PW is placed, the DOS $\rho_{\rm b}$ [the red dashed curve in Fig. 2(e)] shows a sharp peak in the central position of the PW and the peak height decays exponentially with the increased layer. Away from the bottom PW, the DOS $\rho_{\rm b}$ almost overlaps with $\rho_{\rm no}$, indicating that the influence of the single PW is just local [29].

Figure 2(f) shows the DOS $\rho_{\rm t}$ and $\rho_{\rm tb}$ of the central section with top and top/bottom PWs, respectively. The DOS $\rho_{\rm t}$ is symmetric with $\rho_{\rm b}$ about the central site $i_c=(N_zN_y)/2+1$ because the systems in Figs. 2(b) and 2(c) can be transformed into each other by a combined operation of the time-reversal operator $\hat{T}$ and the twofold rotation C_2^x along the x axis. When the bottom PW is further placed, in addition to a peak in the bottom PW, the DOS inside the top PW shows a dramatic decrease. Meanwhile, the DOS of the bottom PW in turn is also influenced as compared with the peak height of $\rho_{\rm b}$ in Fig. 2(e).

In order to clearly show the nonlocal correlation, we define the DOS differences $\rho_{\mathrm{b}} - \rho_{\mathrm{no}}$ and $\rho_{\mathrm{tb}} - \rho_{\mathrm{t}}$ as the responses of the applied bottom PW and plot them in Fig. 2(g) (also see Appendix B), while, without the top PW, $\rho_{\mathrm{b}} - \rho_{\mathrm{no}}$ is almost zero when deviated from the center of the bottom PW by $3a$. However, in the existence of the top PW, the DOS in the top surface has a giant response to the bottom PW and $\rho_{\mathrm{tb}} - \rho_{\mathrm{t}}$ shows deep valley at the center of the top PW. The bottom PW itself is mutually influenced as a feedback to the top nonlocal response. The giant nonlocal response in the double PWs case indicates that there does exist a remote nonlocal correlation between the top and bottom PWs. Since we have chosen the transport direction in the $\pm x$ direction, the Weyl fermions cannot take a side circle to reach the opposite surface. In addition, the distance between the two Weyl nodes is set to the maximum value π/a by fixing $\gamma = 0$, and the slab thickness is set to $N_y = 20$ in the calculation, so the coupling between the top and surface states is infinitely small. As a result, the only reason for the remote correlation is the Weyl orbit regime we discussed above.

B. Enhancement of the nonlocal transport

Next we show that, except for the DOS response, an enhanced nonlocal transport in a six-terminal system could also be induced by the nonlocal correlation. On the basis of Figs. 2(a), 2(c), and 2(d), we additionally connect four electrodes on the top and bottom surfaces as probing terminals [30,31]. The electrode is composed of two-dimensional normal metals which can be described by a tight-binding Hamiltonian $H_{\mathrm{NM}} = \sum_{i,\sigma} E_0 a_{i\sigma}^\dagger a_{i\sigma} + t_{\mathrm{NM}} \sum_{\langle ij\rangle,\sigma} a_{i\sigma}^\dagger a_{j\sigma}$. Here $a_{i\sigma}^\dagger$ ($a_{i\sigma}$) is the creation (annihilation) operator at site i with spin σ, E_0 is the on-site energy, and $\langle ij\rangle$ denotes the nearest sites with a hopping amplitude t_{NM}. The coupling between the normal metal and the WSM nanoribbon can be described with $H_{\mathrm{coupl}} = t_{\mathrm{coupl}} \sum_{i\in\mathrm{NM},\, j\in\mathrm{WSM},\sigma} a_{i\sigma}^\dagger c_{j\sigma} + \mathrm{H.c.}$, with t_{coupl} the coupling strength. Figure 3(a) shows the right side view of the six-terminal system refitted from Fig. 2(d). The blue lines denote the connected electrodes, the top and bottom red arrows denote the topological surface states, and the yellow circles represent the PWs.

To calculate the transmission coefficients in the six-terminal system, we divide it into six terminals labeled by the index $m =$ front, bottom, 1, 2, 3, 4, and a central region with Hamiltonian H_C. By calculating the self-energies Σ_m^r of the six terminals, the retarded Green's function of the central region is obtained as $\tilde{\mathbf{G}}_C^r(E) = [(E + \tilde{\eta}t)\mathbf{I} - H_C - \sum_m \Sigma_m^r]^{-1}$, with $\tilde{\eta}$ an infinitely small imaginary number. The transmission coefficients T_{mn} from terminal n to terminal m can be obtained by [30]

$$T_{mn}(E) = \mathrm{Tr}\big[\Gamma_m(E)\tilde{\mathbf{G}}_C^r(E)\Gamma_n(E)\tilde{\mathbf{G}}_C^a(E)\big], \tag{4}$$

where $\Gamma_m(E) = i[\Sigma_m^r - (\Sigma_m^r)^\dagger]$ is the linewidth function for terminal m and $\tilde{\mathbf{G}}_C^a(E) = [\tilde{\mathbf{G}}_C^r(E)]^\dagger$ is the advanced Green's function of the central region. In the calculations, we set $E_0 = 0$, $t_{\mathrm{NM}} = t$, and $t_{\mathrm{coupl}} = t$.

We first give the transmission coefficients T_{m1} from terminal 1 to terminal m ($m = 2$, 3, 4, front, and back) without the PWs in Fig. 3(b). For the incident energy $E < 0.21t$, the transmission coefficients T_{41} and T_{b1} have large values, while

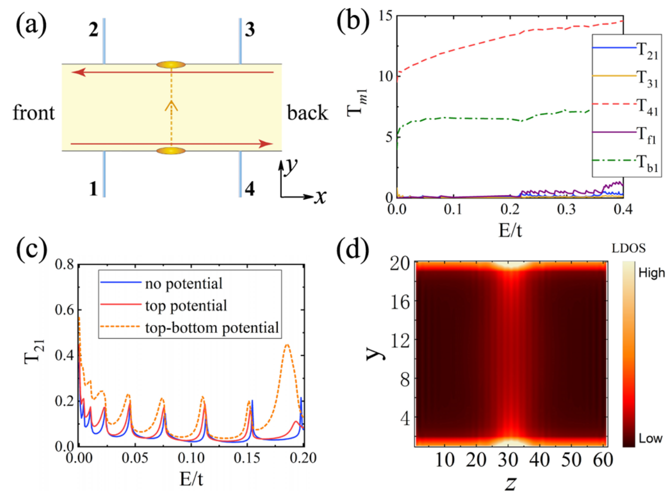

FIG. 3. Nonlocal transport in the six-terminal system. (a) The six-terminal system composed of an infinitely long WSM nanoribbon and four normal metal electrodes which are connected on the top and bottom surfaces. The red arrows denote the propagation of the surface states and the yellow circles mark the positions of the surface PWs. The dashed line between the PWs shows the nonlocal correlation. (b) The transmission coefficients T_{i1} as functions of energy E in the six-terminal system without PWs. (c) The nonlocal transmission coefficient T_{21} for the six-terminal system with no PWs, top PW, and top/bottom PWs, respectively. (d) The DOS profile of the central section in an infinitely long WSM nanoribbon with top/bottom PWs. The energy is set to $E = 0.186t$.

the other transmissions are quite small with their probability being nearly zero. This indicates that almost all the Weyl fermions propagate along the surfaces and the intersurface transport can hardly happen. Further increasing E, T_{21} and T_{f1} have small steplike increases because the second bulk states above the Weyl orbit begin to participate.

In Fig. 3(c) we restrict the transport into the Weyl orbit regime by setting the energy range to $[0, 0.2t]$ and investigate the influence of the surface PWs on the nonlocal transmission T_{21}. In the no-PWs case, T_{21} has small values in most of the energy regions (see the blue curve) except for showing sharp peaks in the Van Hove singularities of the energy band. These Van Hove singularities arise from the finite size effect [32] of the nanoribbon in the z direction, where the momentum p_z is discretized and the energy band which contains the Weyl orbit becomes a series of 1D subbands. Putting a PW on the top surface, T_{21} increases slightly because few electrons in the bulk states are scattered into terminal 2. Further adding a PW on the bottom surface, the transmission coefficient T_{21} shows a dramatic enhancement in the whole energy range $[0, 0.2t]$ (see the dotted yellow curve) with its amplitude serval times larger than the single PW case. This enhancement cannot originate from the normal scattering of the bulk states by two PWs and is a prominent sign for the nonlocal correlation between the top/bottom surfaces. Once the correlation is established by virtue of the Weyl orbit, Weyl fermions propagating in the bottom surface can be pumped into the bulk and then run into the the top surface, which constructs a transmission channel enhancing the nonlocal intersurface transport.

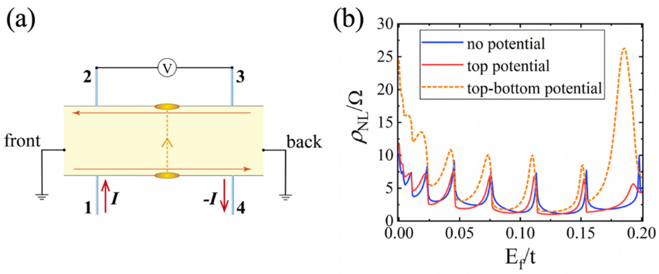

FIG. 4. Experimental observable in the nonlocal transport in the WSM slab. (a) A designed device for experimental observations. Here the front and back terminals are grounded, the terminals 1 and 4 are floured with a constant current I, and the terminals 2 and 3 are connected by an external voltmeter to detect the voltage response V_{23}. (b) The nonlocal resistance ρ_{NL} as a function of the Fermi surface E_f in the six-terminal system.

At a critical energy $E_c = 0.186t$, we note a remarkable transmission peak with its value about seven times that of the single PW case and 13 times that of the no PWs case [see Fig. 3(c)]. Although the peak position is close to the Van Hove singularity of the nearest subband, its appearance cannot be explained by the large DOS from the Van Hove singularity because the height and broadening are both larger than the usual peaks of $E < E_c$. The conductance peak observed in a mesoscopic system always implies the existence of another quantum state. To validate this, we plot the DOS profile of the central section in the infinitely long nanoribbon at energy E_c in Fig. 3(d). The bright fringes in the top and bottom layers of Fig. 3(d) indicate the surface states and the bright spots mark the positions of the two PWs. Between the two PWs, there exists a bright DOS stripe with a bridgelike shape linking the top and bottom surfaces. This suggests a resonant state formed by two spatially separated confining potentials with the wave function spreading to the nonconfined region. We here name it the "Weyl bridge state." Its distribution is quite similar to the worm-hole effect in a 3D topological insulator [33] and the 3D quantum Hall state in the topological semimetals [34]. The most important distinction between them is that the Weyl bridge state does not rely on the globally applied magnetic field and is an intrinsic generation of the exotic topological band structure of WSMs. So the nonlocality discovered here should be unique in topological semimetals with a Weyl orbit structure. Besides, we also want to make a comparison between the Weyl bridge state and a natural phenomenon of lightning: if there accumulate enough free charges in the cloud, putting a conductor in the ground would induce an electric breakdown through the atmosphere. In our WSM systems, the top/bottom PWs play the role of the cloud and the conductor, respectively, and the Weyl bridge state is just a breakdown of Weyl fermions through the WSM body.

The six-terminal system in Fig. 3(a) can be further improved into an experimental device for measuring the nonlocal transport signal, as shown in Fig. 4(a). Similar to a Coulomb drag system [35], we make the front and back terminals grounded, pour a constant current I in terminals 1 and 4, and connect an external voltmeter between terminals 2 and 3 to measure the responsive voltage $V_{23} \equiv V_2 - V_3$. We then define the nonlocal resistance $\rho_{\mathrm{NL}} \equiv V_{23}/I$ as an experimental observable. Using the Landauer-Büttiker formula, we obtain the nonlocal resistance as a function of the Fermi energy E_f (relative to the energy of the Weyl nodes), which is shown in Fig. 4(b). The result is very similar to that in Fig. 3(c) and shows that the nonlocal resistance is greatly enhanced once the top/bottom PWs are both placed on the slab surfaces. The dramatic resistance peak at $E = 0.186t$ implies the Weyl bridge state. These observations can serve as evidence for verifying the nonlocal correlation mediated by the Weyl orbit in experiments.

IV. SEMICLASSICAL DESCRIPTION

In this section we give a semiclassical description on the trajectories of the Weyl fermions confined by the top/bottom PWs and explain the appearance of the Weyl bridge state. We first consider a continuous model to describe the Weyl orbit. Between the two Weyl nodes, the surface states can be described by an effective Hamiltonian or dispersion [27]:

$$E = \pm\hbar v k_x, \quad -k_0 < k_z < k_0. \tag{5}$$

Here $\pm v$ is the group velocity of the bottom (top) surface states and $v = ta/\hbar$ under the tight-binding model parameters. The bulk states near the Weyl nodes can be described by the dispersion:

$$E = \hbar\sqrt{v^2k_x^2 + v_z^2(k_z \pm k_0)^2 + v^2k_{y0}^2}, \quad |k_z| > k_0. \tag{6}$$

Here the Fermi velocity $v_z = ta \sin k_0a/\hbar$ is obtained by expanding $H(\mathbf{k})$ around the Weyl nodes and k_{y0} is the minimum wave vector in the y direction, which can be approximated as $\pi/(N_y + 1)a$.

Meanwhile, without the PWs, both the surface states and bulk states in Eqs. (5) and (6) are eigenstates of the WSM slab and they are decoupled. But in the existence of the PWs the electrostatic force of the PWs can drive the Weyl fermion to move in momentum space. We consider the Weyl fermion trapped inside the top PW. Its semiclassical equations of motion can be written as

$$\begin{aligned} \mathbf{\Pi} &= \partial_{\mathbf{k}}E(\mathbf{k})/\hbar, \\ \hbar d\mathbf{k}/dt &= \mathbf{F} = -\partial_{\mathbf{r}}U(\mathbf{r}), \end{aligned} \tag{7}$$

where $\mathbf{\Pi}$ is the semiclassical velocity, and the effect of the Berry curvature which arises from the multiband property of the band structure has been ignored. More specifically, Eq. (7) can be rewritten into the following two-component forms:

$$\begin{aligned} \Pi_x &= \partial_{k_x}E(\mathbf{k})/\hbar, \quad \Pi_z = \partial_{k_z}E(\mathbf{k})/\hbar, \\ \hbar dk_x/dt &= -2\omega_x x, \quad \hbar dk_z/dt = -2\omega_z z. \end{aligned} \tag{8}$$

Once the initial position $\mathbf{r}_0 = (x_0, z_0)$ and the initial wave vector $\mathbf{k}_0 = (k_{x0}, k_{z0})$ at time $t = 0$ are known, the momentum space position (k_x, k_z) in the Weyl orbit and the real space position (x, z) can be solved by Eq. (8). The y-component coordinate of the Weyl fermion is estimated by calculating the expectation of the operator $\hat{y}$ for the eigenstate on the Weyl orbit with wave vector (k_x, k_z). Therefore, the trajectory of the Weyl fermions inside the slab is hence determined.

Next let us consider one specific trajectory which is closed in both real and momentum space and forms the Weyl bridge

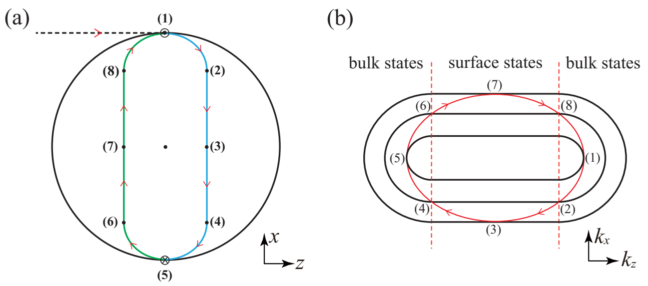

FIG. 5. Semiclassical trajectories of the Weyl bridge state. (a) Planform of the real-space trajectory for Weyl fermions confined in the WSM slab. The Weyl fermion first comes in from position (1) on the top surface, then passes the positions (2–8), and finally moves from position (8) back into the original position (1) to accomplish one enclosed loop which stretches across the whole WSM slab. Here the right blue curve denotes the trajectory on the top surface and the left green curve denotes the trajectory on the bottom surface. On the connections of the top and bottom curves, the Weyl fermion realized a tunneling between the top and bottom surfaces. (b) The enclosed trajectory (red curve) in the momentum space, corresponding to positions (1–8) in (a). Here the black enclosed curves denote the isoenergetic Weyl orbits. Note that in Fig. 1(b) we only show one Weyl orbit with equal energy, but in the real motion the trajectory is not isoenergetic due to the confined potential and goes through many Weyl orbits, as shown in (b).

state. We consider that the Weyl fermion is incident from position (1) on the top surface [see the planform of the WSM slab in Fig. 5(a)], i.e., incident from the bulk state with initial position $(r_0, 0)$ and initial wave vector $(0, k_{z0})$ [see the corresponding momentum position in Fig. 5(b)]. Once the Weyl fermion is captured by the PW, its real-space trajectory will deflect due to the attractive electrostatic force, and then arrives at position (2) and the Weyl fermion thus migrates to the surface state. After position (2), due to $\Pi_z = \partial_{k_z} E(\mathbf{k})/\hbar = 0$ on the surface, the Weyl fermion moves in $-x$ direction straight with the velocity $(-v, 0)$ from position (2) to position (4), as shown in Fig. 5(a). Here, due to the persistent attraction in the $-z$ direction and both $\hbar dk_x/dt = -2\omega_x x$ and $\hbar dk_z/dt = -2\omega_z z$ being nonzero, the Weyl fermion moves leftwards in the momentum space from position (2) to position (3) along the elliptical trajectory [see Fig. 5(b)]. If the change of the wave vector k_z during the motion from (1) to (3) satisfies

$$\Delta k_z = k_0, \tag{9}$$

where k_0 is the half-distance between the two Weyl nodes, the Weyl fermion will accomplish the following motion: moving from position (3) to (4) to get back to the bulk state, revolving in the real-space to immigrate to position (5), tunneling from the top surface to the bottom one, and then moving from (5) to (1) passing positions (6), (7), and (8) by repeating the motion (1-2-3-4-5). Finally, the Weyl fermion tunnels from the bottom surface to the top one and gets back to its original position. The real-space and momentum-space trajectories are therefore enclosed. If the phase accumulated during the enclosed loop is an integer multiples of 2π, a stationary state (i.e., a Weyl bridge state we discussed in Sec. III) appears, which results in the strong nonlocal correlation effect.

V. DISCUSSION AND CONCLUSION

Experimentally the surface PW can be generated by an impurity [36] or STM tip potential [37,38]. By preparing the four samples in Fig. 2 and measuring the DOS response with an STM tip, or performing a transport measurement on the basis of Fig. 4, the aforementioned nonlocal correlation can be easily verified. In our calculations we have set the radius of the PW to be about 10 times that of the lattice constant a. However, with an STM tip the radius of the PW can be regulated into 100 times that of a (assuming that $a = 1$ nm) [39,40], so the nonlocal signal observed in experiments can be greatly enhanced compared with the presented numerical results. Since the nonlocal correlation is transmitted through the bulk states on the Weyl orbits, disorder can obstruct the intersurface transport due to the scattering. So to make the nonlocal effect prominent, the thickness of experimental samples should be smaller than the mean free path of Weyl fermions. Besides, in choosing the proper WSM material, a long distance between the Weyl nodes in momentum space is demanded. The reason is that, once the two Weyl nodes are close with each other, the coupling between the top and bottom surface Fermi arcs becomes strong and would cause a similar nonlocal effect, which masks the nonlocality arising from the Weyl orbits.

To conclude, we have proven a nonlocal correlation effect in WSMs as a result of the Weyl orbit. As a unique property of topological semimetals, this nonlocal correlation is totally mediated by the quantum states residing on the Weyl orbit and can be simply generated by two surface PWs. A lightninglike bridge state is found to exist through the WSM body which makes the nonlocal correlation strongest. The movable PWs allow a flexible and precise engineer on this nonlocal correlation and provide a way to investigate the surface-bulk relationship in topological semimetals. The present result adds another member in the family of nonlocal phenomena and has guiding significance in designing unique electric devices with fancy functions, such as the impurity detection and remote control in mesoscopic and microscales.

ACKNOWLEDGMENTS

Z.H. acknowledges helpful discussions with H. Jiang. This work was financially supported by National Key R & D Program of China (Grant No. 2017YFA0303301), NSF-China (Grant No. 11921005), the Strategic Priority Research Program of Chinese Academy of Sciences (Grant No. DB28000000), and Beijing Municipal Science & Technology Commission (Grant No. Z191100007219013).

APPENDIX A: EVOLUTION OF THE WAVE FUNCTIONS IN THE WEYL ORBIT

In this Appendix we discuss the wave-function evolution of the Weyl orbit to see how the wave function is pumped from the top surface into the bottom one. In Fig. 6(a) we select six points on the Weyl orbit and plot their corresponding wave functions in Fig. 6(b). For the top surface state 1, its wave function is localized on the top layer and decays quickly into zero after one-layer distance away from the surface. Under the drive of the top PW, the wave function gradually evolves

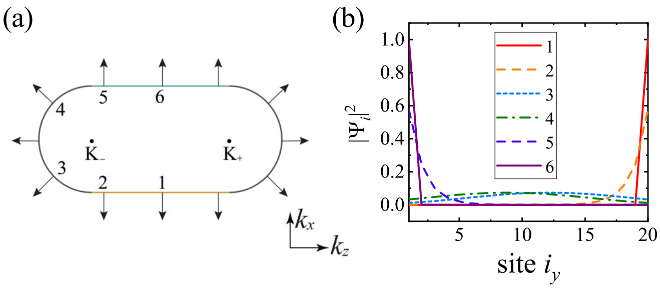

FIG. 6. (a) Weyl orbit with two Weyl nodes $\mathbf{K}_\pm$ enclosed inside. (b) The square modulus of the wave functions 1–6 picked from (a) distributing in the slab thickness direction y. The energy is chosen as $E = 0.2t$, and the wave vectors (k_x, k_z) of the states 1(6), 2(5), and 3(4) are set as $(\pm 0.201/a, 0)$, $(\pm 0.201/a, -1.194/a)$, and $(\pm 0.099/a, -1.696/a)$, respectively.

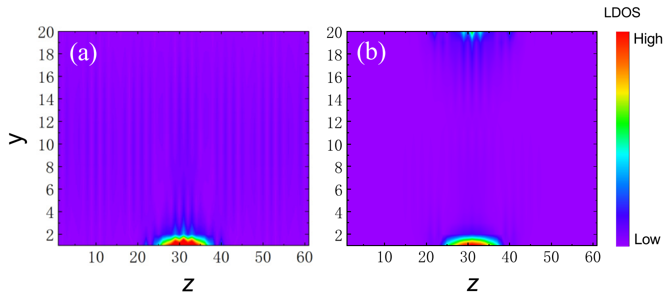

FIG. 7. DOS response in the central section of the WSM slab. (a),(b) The DOS change $|\rho_b - \rho_{no}|$ and $|\rho_{tb} - \rho_t|$. The parameters are the same as those in Fig. 2 in Sec. III.

into state 2 with its broadening about two or three layers long. Further driving the wave function, the surface state is pushed out of the topological region connected by the two Weyl nodes $\mathbf{K}_\pm$ and becomes bulk state 3. Here the wave function is distributed over the whole body of the WSM slab with few amplitudes permeating into the bottom surface. Once the bottom PW is placed, the local electrostatic force will continue driving wave function 3 by acting on its bottom surface part and then the wave function is pumped into states 4, 5, and 6 sequentially. Finally, top surface state 1 is pumped into bottom surface state 6 under the assistance of both the top/bottom PWs.

APPENDIX B: RESPONSE OF THE DOS IN THE WSM NANORIBBON SHOWN WITH COLOR

In Figs. 2(e)–2(g) of Sec. III, we show the DOS versus the site index i, where the site $i = i_z + (i_y - 1)N_z$ counts from the left to the right and then from the bottom to the top. Figure 7 shows the same DOS change $|\rho_b - \rho_{no}|$ and $|\rho_{tb} - \rho_t|$ versus the site (i_z, i_y), but here the DOS is represented by color.

[1] A. Einstein, B. Podolsk, and N. Rosen, Can quantum-mechanical description of physical reality be considered complete? Phys. Rev. **47**, 777 (1935).
[2] R. Horodecki, P. Horodecki, M. Horodecki, and K. Horodecki, Quantum entanglement, Rev. Mod. Phys. **81**, 865 (2009).
[3] J. S. Bell, On the Einstein Podolsky Rosen paradox, Physics **1**, 195 (1964).
[4] N. Gisin, Bell's inequality holds for all non-product states, Phys. Lett. A **154**, 201 (1991).
[5] S. Popescu, Nonlocality beyond quantum mechanics, Nat. Phys. **10**, 264 (2014).
[6] C. H. Bennett and S. J. Wiesner, Communication via One- and Two-particle Operators on Einstein-Podolsky-Rosen States, Phys. Rev. Lett. **69**, 2881 (1992).
[7] C. H. Bennett, G. Brassard, C. Crépeau, R. Jozsa, A. Peres, and W. K. Wootters, Teleporting an Unknown Quantum State via Dual Classical and Einstein-Podolsky-Rosen Channels, Phys. Rev. Lett. **70**, 1895 (1993).
[8] A. Y. Kitaev, Unpaired Majorana fermions in quantum wires, Phys. Usp. **44**, 131 (2001).
[9] L. Fu and C. L. Kane, Superconducting Proximity Effect and Majorana Fermions at the Surface of a Topological Insulator, Phys. Rev. Lett. **100**, 096407 (2008).
[10] R. M. Lutchyn, J. D. Sau, and S. Das Sarma, Majorana Fermions and a Topological Phase Transition in Semiconductor-Superconductor Heterostructures, Phys. Rev. Lett. **105**, 077001 (2010).
[11] J. Klinovajia and D. Loss, Fractional charge and spin states in topological insulator constrictions, Phys. Rev. B **92**, 121410(R) (2015).
[12] J. Alicea, Y. Oreg, G. Refael, F. von Oppen, and M. P. A. Fisher, Non-Abelian statistics and topological quantum information processing in 1D wire networks, Nat. Phys. **7**, 412 (2011).
[13] Y. Wu, H. Liu, J. Liu, H. Jiang, and X. C. Xie, Double-frequency Aharonov-Bohm effect and non-Abelian braiding properties of Jackiw-Rebbi zero-mode, Nat. Sci. Rev. **7**, 572 (2020).
[14] A. L. Fetter and J. D. Walecka, Screening in an electron gas, in *Quantum Theory of Many-Particle Systems* (McGraw-Hill Book Company, New York, 1971), pp. 175–180.
[15] P. J. W. Moll *et al.*, Transport evidence for Fermi-arc-mediated chirality transfer in the Dirac semimetal Cd_3As_2, Nature (London) **535**, 266 (2016).
[16] C. Zhang *et al.*, Evolution of Weyl orbit and quantum Hall effect in Dirac semimetal Cd_3As, Nat. Commun. **8**, 1272 (2017).
[17] C. Zhang *et al.*, Quantum Hall effect based on Weyl orbits in Cd_3As_2, Nature (London) **565**, 331 (2019).
[18] X. Wan, A. M. Turner, A. Vishwanath, and S. Y. Savrasov, Topological semimetal and Fermi-arc surface states in the electronic structure of pyrochlore iridates, Phys. Rev. B **83**, 205101 (2011).
[19] A. A. Burkov and L. Balents, Weyl Semimetal in a Topological Insulator Multilayer, Phys. Rev. Lett. **107**, 127205 (2011).
[20] S.-Y. Xu *et al.*, Discovery of a Weyl fermion semimetal and topological Fermi arcs, Science **349**, 613 (2015).
[21] B. Q. Lv *et al.*, Experimental Discovery of Weyl Semimetal TaAs, Phys. Rev. X **5**, 031013 (2015).
[22] S.-M. Huang *et al.*, A Weyl fermion semimetal with surface Fermi arcs in the transition metal monopnictide TaAs class, Nat. Commun. **6**, 7373 (2015).

[23] Q.-D. Jiang, H. Jiang, H. Liu, Q.-F. Sun, and X. C. Xie, Topological Imbert-Fedorov Shift in Weyl Semimetals, Phys. Rev. Lett. **115**, 156602 (2015).
[24] C.-Z. Chen, J. Song, H. Jiang, Q.-F. Sun, Z. Wang, and X. C. Xie, Disorder and Metal-Insulator Transitions in Weyl Semimetals, Phys. Rev. Lett. **115**, 246603 (2015).
[25] Z. Hou, Y.-F. Zhou, N.-X. Yang, and Q.-F. Sun, Chirality-dependent electron transport in Weyl semimetal p-n-p junctions, Commun. Phys. **2**, 86 (2019).
[26] N.-X. Yang, Y.-F. Zhou, Z. Hou, and Q.-F. Sun, Anomalous spin Nernst effect in Weyl semimetals, J. Phys.: Condens. Matter **31**, 435301 (2019).
[27] C. M. Wang, H.-P. Sun, H.-Z. Lu, and X. C. Xie, 3D Quantum Hall Effect of Fermi Arcs in Topological Semimetals, Phys. Rev. Lett. **119**, 136806 (2017).
[28] Y. Xu *et al.*, Observation of topological surface state quantum Hall effect in an intrinsic three-dimensional topological insulator, Nat. Phys. **10**, 956 (2014).
[29] P. Hosur, Friedel oscillations due to Fermi arcs in Weyl semimetals, Phys. Rev. B **86**, 195102 (2012).
[30] Z. Hou, Y. Xing, A.-M. Guo, and Q.-F. Sun, Crossed Andreev effects in two-dimensional quantum Hall systems, Phys. Rev. B **94**, 064516 (2016).
[31] S. Datta, *Electronic Transport in Mesoscopic Systems* (Cambridge University Press, Cambridge, UK, 1995).
[32] S. Das Sarma and X. C. Xie, Calculated transport properties of ultrasubmicrometer quasi-one-dimensional inversion lines, Phys. Rev. B **35**, 9875(R) (1987).
[33] G. Rosenberg, H.-M. Guo, and M. Franz, Wormhole effect in a strong topological insulator, Phys. Rev. B **82**, 041104(R) (2010).
[34] Y. Zhang, D. Bulmash, P. Hosur, A. C. Potter, and A. Vishwanath, Quantum oscillations from generic surface Fermi arcs and bulk chiral modes in Weyl semimetals, Sci. Rep. **6**, 23741 (2016).
[35] B. N. Narozhny and A. Levchenko, Coulomb drag, Rev. Mod. Phys. **88**, 025003 (2016).
[36] F. Ghahari *et al.*, An on/off Berry phase switch in circular graphene resonators, Science **356**, 845 (2017).
[37] J. Lee *et al.*, Imaging electrostatically confined Dirac fermions in graphene quantum dots, Nat. Phys. **12**, 1032 (2016).
[38] Y. Zhao *et al.*, Creating and probing electron whispering-gallery modes in graphene, Science **348**, 672 (2015).
[39] N. M. Freitag *et al.*, Electrostatically confined monolayer graphene quantum dots with orbital and valley splittings, Nano Lett. **16**, 5798 (2016).
[40] Y.-W. Liu, Z. Hou, S.-Y. Li, Q.-F. Sun, and L. He, Movable Valley Switch Driven by Berry Phase in Bilayer Graphene Resonators, Phys. Rev. Lett. **124**, 166801 (2020).